The Astrophysical Journal, 657:1172 – 1177, 2007 March 10

WAVELENGTH MEASUREMENTS OF Ni L-SHELL LINES BETWEEN 9 AND 15 Å

M. F. Gu,[1] P. Beiersdorfer,[2] G. V. Brown,[2] H. Chen,[2] D. B. Thorn,[2] and S. M. Kahn[1]

Received 2006 October 10; accepted 2006 November 20

ABSTRACT

We present accurate wavelength measurements of nickel L-shell X-ray lines resulting from $\Delta n \geq 1$ transitions between 9 and 15 Å. We have used the electron beam ion trap, SuperEBIT, at the Lawrence Livermore National Laboratory and a flat-field grating spectrometer to record the spectra. The most significant emission lines of Ni XIX–XXVI in our spectral coverage are identified, and their relative intensities are determined. The resulting data set provides valuable input for the analyses of high-resolution X-ray spectra of stellar coronae sources, including the Sun.

Subject headings: atomic data — line: identification — stars: coronae — Sun: corona — Sun: X-rays, gamma rays — X-rays: general

1. INTRODUCTION

A complete line list with accurate wavelengths and emissivities is an indispensable tool for X-ray spectroscopic analyses. High-resolution observations with the grating spectrometers on board *Chandra* and *XMM-Newton* have made it possible to study numerous individual soft X-ray lines for density and temperature diagnostics. Many of these lines are located in a crowded spectral region between 8 and 20 Å, which includes K-shell emission of H-like and He-like ions of O, Ne, and Mg and L-shell emissions of Fe and Ni ions. Accurate measurements of line fluxes for either emission measure analyses or density diagnostics require careful modeling of blending features in many situations. Such modeling can be carried out reliably only if the wavelengths of contributing lines are known to a high degree of accuracy.

The wavelengths of H-like and He-like lines have been known with sufficient accuracy for applications in X-ray spectroscopy with the grating spectrometers on board *Chandra* and *XMM-Newton* (Johnson & Soff 1985; Drake 1988). Systematic line surveys of Fe L-shell lines have been completed only recently. Brown et al. (1998) gave a complete list of Fe XVII lines above 10 Å, including $n \rightarrow 2$ transitions for $n \leq 10$. Brown et al. (2002) extended the line list with transitions from Fe XVIII to XXIV between 10.6 and 18 Å. Chen et al. (2007) made further wavelength measurements of Fe L-shell emissions down to 6 Å, most of which are high-n transitions to the $n = 2$ configurations. All these measurements were carried out at the University of California Lawrence Livermore National Laboratory (LLNL) using the electron beam ion trap facilities, EBIT-I and EBIT-II.

The L-shell lines from Ni ions are considerably weaker than the corresponding Fe lines in the X-ray spectra of astrophysical sources due to the much lower cosmic abundance of Ni. Nevertheless, prominent Ni lines have been identified in the solar X-ray spectra obtained with the Flat Crystal Spectrometer aboard the *Solar Maximum Mission* (Phillips et al. 1982). The Ne-like Ni XIX lines are also routinely detected in the *Chandra* spectra of stellar coronae. The inclusion of these lines in models provides important constraints on the Ni abundance measurements. With ever-increasing sensitivity of next-generation X-ray observatories, such as *Constellation-X*, the modeling of weaker lines from other Ni L-shell ions can become important as well, not only because the deblending of these emissions from neighboring Fe lines is essential to utilize Fe line diagnostics, but also because these lines provide additional constraints on the density and emission measure distribution.

In this paper, we present a systematic wavelength survey of Ni L-shell lines between 9 and 15 Å. The details of the experiment are described in § 2, data analysis and line identifications are discussed in § 3, § 4 presents the entire line list and a short discussion of the measured line intensities, and a brief summary is given in § 5.

2. MEASUREMENT

The measurements were carried out using the SuperEBIT electron beam ion trap facility at LLNL, employing a high-resolution flat-field grating spectrometer. The details of the Livermore electron beam ion traps have been described elsewhere (Levine et al. 1988; Beiersdorfer 2003), and the implementation and performance of the grating spectrometer can be found in Beiersdorfer et al. (2004).

Ni was injected in form of $(C_5H_5)_2Ni$, i.e., bis(cyclopentadienyl)-nickel, using a differential gas injection system. The injected ions were trapped for about 0.7 s in each cycle. The relatively short injection cycle was chosen to avoid accumulation of heavy ion contaminations. Data were taken at several electron beam energies ranging from 1.6 to 3.3 keV to select specific Ni L-shell charge states for study. The beam current was set at ~10 mA throughout these measurements, giving an electron density of $\sim 10^{11}$–10^{12} cm^{-3} in the trap region depending on the beam energy and current. Such densities are considered to be coronal limits for Ni L-shell ions so that all emission lines are produced by collisional excitation from the ground state and the subsequent radiative cascades.

The spectra were recorded on a two-dimensional charge-coupled device (CCD) with 1300×1340 pixels. The total data collection time for each energy setting was typically 240 minutes achieved in four separate exposures. Each exposure is filtered for cosmic-ray events and summed to give the total spectrum. Two experimental campaigns were conducted. In the first campaign, there was significant contamination from lines of unknown heavy ions at most electron energies except for $E = 3.26$ keV. In the second campaign, that contamination was no longer present. However, a slight mismatch between the CCD and grating orientation in the second campaign resulted in a somewhat degraded spectral resolution. Nevertheless, the resolving power was sufficiently high to identify major Ni L-shell transitions. In the present analysis, we used seven energy settings from the second

[1] Kavli Institute for Particle Astrophysics and Cosmology and Department of Physics, Stanford University, Stanford, CA.
[2] High Temperature and Astrophysics Division, Physics and Advanced Technologies, Lawrence Livermore National Laboratory, Livermore, CA.

campaign, at 1.63, 1.73, 1.88, 1.98, 2.04, 2.25, and 3.25 keV, and supplemented it with the 3.26 keV setting from the first campaign. The energies quoted here correspond to the total voltages applied to the middle drift tube of the SuperEBIT and do not take into account the space charge potential of the electron beam, which may lower the energies by 50–100 eV. The exact values of electron energies are of no particular importance in the present wavelength measurements, and no absolute calibration procedures were carried out to determine them accurately. These energies were chosen to successively ionize Ni into higher charge states for individual study.

The wavelength calibration was achieved using He-like and H-like Ne lines. More specifically, the H-like Lyα line at 12.135 Å and the He-like lines w (13.447 Å), z (13.699 Å), Kβ (11.547 Å), and Kγ (11.000 Å) were used. These wavelengths are obtained from the atomic spectra database at the National Institute of Standards and Technology (NIST). Because accurate calculations including quantum electrodynamics effects and full account of electronic correlation exist for H-like lines and $2 \rightarrow 1$ transitions of He-like lines (Johnson & Soff 1985; Drake 1988), the uncertainties of the Lyα, w, and z lines are assumed to be less than 1 mÅ. The accuracies of higher n transitions of He-like ions are slightly worse than for the $2 \rightarrow 1$ transitions, and the uncertainties of the Kβ and Kγ lines are assumed to be less than 3 mÅ. For the spectral region below 11 Å, we used three Li-like Ni XXVI lines at 9.060, 9.529, and 9.745 Å as additional calibration lines. For the spectral region above 13.7 Å, we supplemented the calibration line list with two Ne-like Ni XIX lines at 14.043 and 14.077 Å. The wavelengths of these five lines are taken from the many-body perturbation (MBPT) calculation of Gu (2005). Experiences with Fe L-shell lines have shown that the MBPT method gives accurate wavelengths to within 10 mÅ for general open L-shell ions, but the results for Li-like and Ne-like ions are much better. The MBPT wavelengths of Li-like and Ne-like Fe lines agree with the measurements of Brown et al. (1998, 2002) to within 3 mÅ. Therefore, we estimate that the uncertainty introduced by using these calibration lines from Li-like and Ne-like Ni is about 3 mÅ.

3. ANALYSIS AND LINE IDENTIFICATIONS

With the gas injection system, a continuous stream of neutral Ni atoms is supplied to the trap. Therefore, even at very high electron energies, low charge states of Ni ions typically coexist with the higher charge states. The accurate identification of transitions relies on the appearance of new lines in the spectra taken at successively higher electron energies, as described in earlier measurements using gas injection (e.g., Lepson et al. 2002). We used a sophisticated model to ascertain the degree of blending and its effect on wavelength measurements, which we describe below.

We have constructed collisional radiative models for individual Ni L-shell ions under the monoenergetic electron collision condition. Excitations from the ground state of each ion to configurations with $n \leq 7$ are included. The atomic data needed, including level energies, collision strengths, and radiative transition rates, are calculated with the Flexible Atomic Code (FAC) developed in Gu (2003). The theoretical wavelengths for the $3 \rightarrow 2$ transitions are taken from Gu (2005). The computed spectra for individual charge states are properly weighted to fit the observed data, with the weighting coefficients taken as free parameters. During the spectral fit, we use a flat efficiency curve for the spectrometer and Gaussian line profiles with fixed widths, which are determined by fitting a few isolated lines. The overall good agreement between the theoretical and experimental spectra indicates that no obvious contamination is present in these measurements. As an example, the fit to the spectrum taken at 1.98 keV is illustrated in Figure 1. Lines from N-like, O-like, F-like, and Ne-like ions dominate this spectrum. The best-fit relative abundances for these ions are 0.15, 0.72, 0.08, and 0.05, respectively. We note that in the construction of these theoretical spectra, we vary only the relative abundances of ions, with line positions and intensities fixed at the calculated values. The comparison of such theoretical spectra with the measured ones allows us to identify major transitions in each spectrum that have not appeared in the data collected at lower energies. We then fit individual identified transitions with multi-Gaussian components in the local spectral region with centroids and heights as free parameters to measure the wavelengths and intensities. For the spectrum at 1.98 keV, we measure the wavelengths and identify the transitions for six N-like lines. Although the spectrum contains many more lines from lower charge states, these lines are measured and identified using the spectra taken at lower energies.

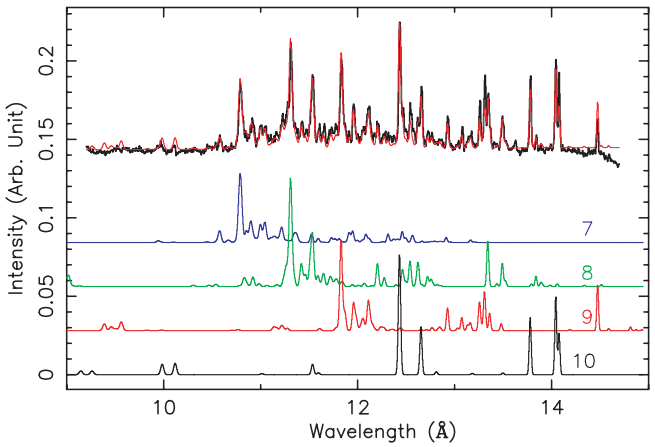

FIG. 1.—Ni L-shell spectrum at the electron energy of 1.98 keV. The top black line is the measured data. The top red line is the theoretical model with relative abundances of N-like, O-like, F-like, and Ne-like ions adjusted to fit the data. The bottom four curves are contributions from individual charge states, with the labels indicating the number of electrons of the ions.

4. RESULTS

In the present work, weak lines from high charge states typically cannot be measured due to heavy blending with lines from lower charge states. Blending in the Ne-like, F-like, and O-like spectra is less severe, and a large number of lines from these charge states are obtained in the present analysis. For higher charge states, only 2–6 lines per ion are measured. Because our spectrometer was better focused, the spectrum taken at 3.26 keV in our first experimental campaign has a higher resolving power, and we use that spectrum to measure several Li-like, Be-like, B-like, and N-like lines, which are more difficult to measure in the spectra taken in the second campaign due to line blending. The identifications of all measured lines are shown in Figures 2, 3, 4, and 5 and listed in Table 1. The wavelength uncertainties given in the table represent the quadrature sum of calibration errors of 3 mÅ and estimated statistical uncertainties, which range from less than 1 mÅ for strong lines to 4 mÅ for weak or blended lines. The experimental and theoretical intensities are given on the scale where the strongest transition of each charge state is 100. The theoretical wavelengths obtained with the configuration interaction theory implemented in FAC and those from the MBPT theory of Gu (2005) are also listed for comparison. For Ne-like lines, we employ the labeling convention

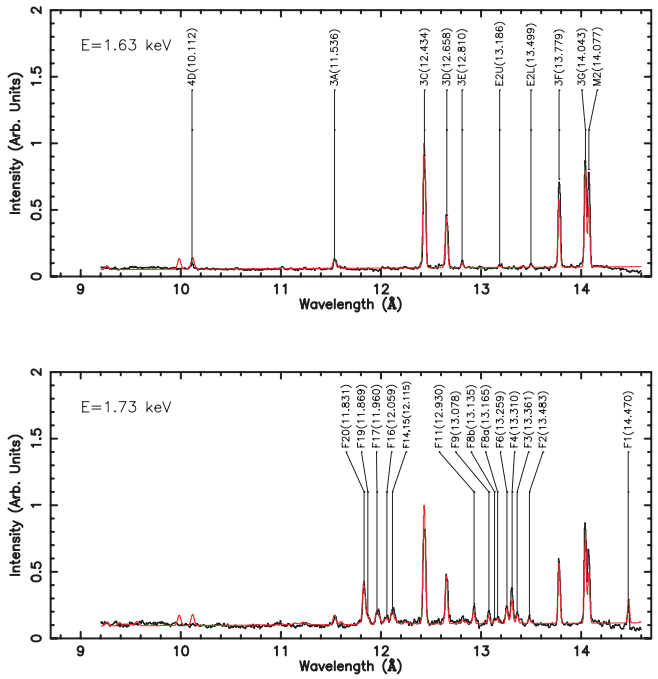

FIG. 2.—Ni L-shell spectra at the electron energies of 1.63 and 1.73 keV and line identifications. The black line is the measured data. The red line is the theoretical model with relative abundances of ions adjusted to fit the data. The line labels correspond to those in Table 1, and the numbers in the parentheses of the labels are the measured wavelengths in angstroms.

of Parkinson (1973) as modified by Beiersdorfer et al. (1988), which was also used in Brown et al. (1998). For other charge states from Ni XX to XXIV, the line labels are matched to those of the corresponding transitions of Fe XVIII–XXIV given in Brown et al. (2002).

The present work measures fewer lines than in Brown et al. (2002), and for some lines, the transitions identified here are different from those of the corresponding Fe lines. Some of these discrepant identifications are due to the different configuration interactions included in the theoretical calculations used in the analyses. Brown et al. (2002) used the Hebrew University Lawrence Livermore Atomic Code (HULLAC; Bar-Shalom et al. 2001), while the present work uses FAC. Moreover, the slightly different atomic numbers for Ni and Fe also cause differences in the configuration interaction. In theoretical calculations, an atomic

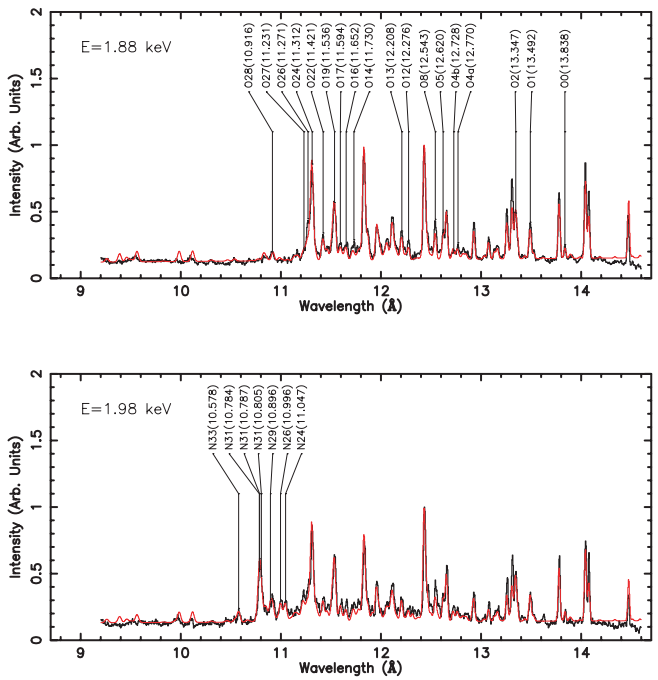

FIG. 3.—Same as Fig. 2, except at electron energies of 1.88 and 1.98 keV.

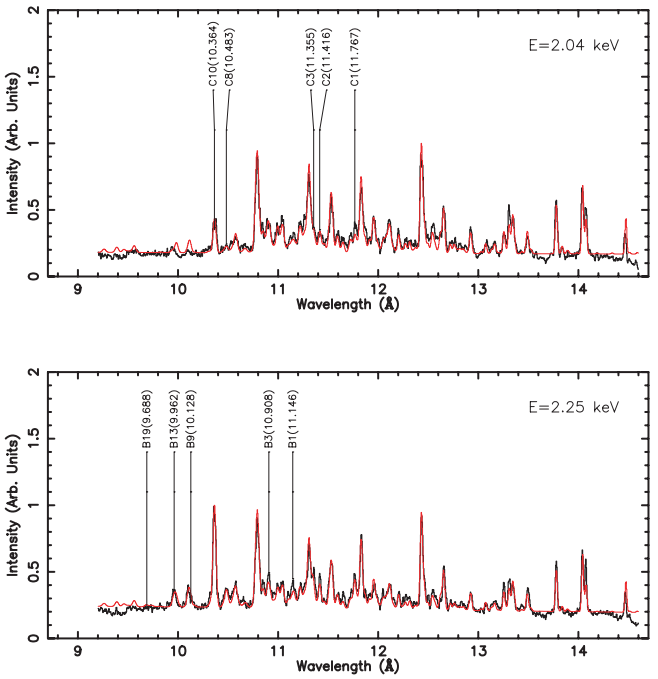

FIG. 4.—Same as Fig. 2, except at electron energies of 2.04 and 2.25 keV.

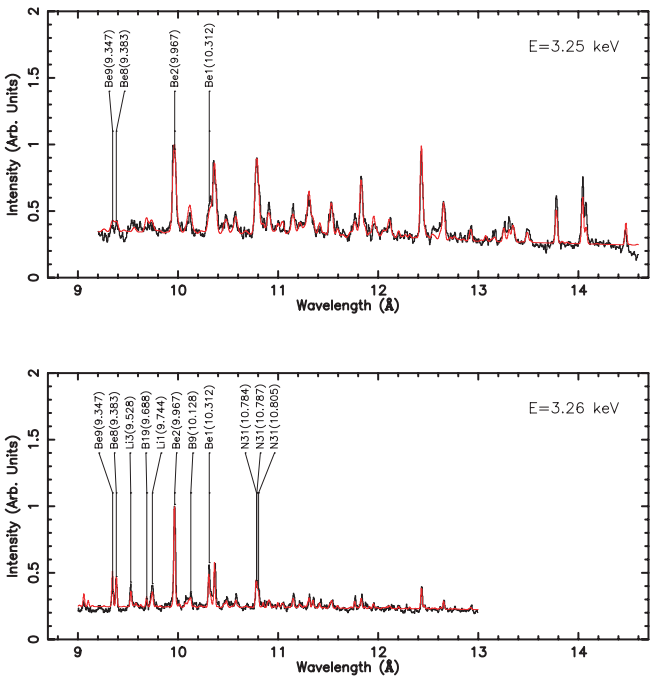

FIG. 5.—Same as Fig. 2, except at electron energies of 3.25 and 3.26 keV. The spectrum at 3.26 keV was taken in a different experimental campaign from all previous spectra, when the grating spectrometer was cut off at 13 Å and had better spectral resolution.

TABLE 1

WAVELENGTHS OF X-RAY LINES FROM Ni XIX TO Ni XXVI

Label[a] (1)	λ_{exp}[b] (Å) (2)	I_{exp}[c] (3)	λ_{CI}[d] (4)	λ_{MBPT}[e] (5)	I_{cal}[f] (6)	Lower[g] (7)	Upper[h] (8)	Phillips[i] (Å) (9)	NIST[j] (Å) (10)
M2	14.077(3)	65.1	14.100	14.077	43.4	$2p_{3/2}^4(J=0)$	$2p_{3/2}^3 3s_{1/2}(J=2)$	14.076	14.077
3G	14.043(3)	77.9	14.062	14.043	65.0	$2p_{3/2}^4(J=0)$	$2p_{3/2}^3 3s_{1/2}(J=1)$	14.041	14.043
3F	13.779(3)	65.1	13.800	13.779	53.0	$2p_{3/2}^4(J=0)$	$2p_{1/2}3s_{1/2}(J=1)$	13.777	13.779
E2L	13.499(5)	3.9	13.515	13.497	1.8	$2p_{3/2}^4(J=0)$	$2p_{3/2}^3 3p_{1/2}(J=2)$	...	...
E2U	13.186(5)	6.1	13.199	13.181	1.6	$2p_{3/2}^4(J=0)$	$2p_{1/2}3p_{3/2}(J=2)$	...	...
3E	12.810(5)	10.5	12.827	12.810	4.3	$2p_{3/2}^4(J=0)$	$2p_{3/2}^3 3d_{3/2}(J=1)$	...	12.812
3D	12.658(3)	46.2	12.666	12.653	37.7	$2p_{3/2}^4(J=0)$	$2p_{3/2}^3 3d_{5/2}(J=1)$	12.652	12.656
3C	12.434(3)	100.0	12.438	12.432	100.0	$2p_{3/2}^4(J=0)$	$2p_{1/2}3d_{3/2}(J=1)$	12.430	12.435
3A	11.536(5)	6.7	11.518	11.536	8.5	$2p_{3/2}^4(J=0)$	$2s_{1/2}3p_{3/2}(J=1)$	...	11.539
4D	10.112(5)	5.4	10.118	...	12.6	$2p_{3/2}^4(J=0)$	$2p_{3/2}^3 4d_{5/2}(J=1)$	...	10.110
F1	14.470(5)	31.0	14.480	14.475	36.9	$2s_{1/2}(J=\frac{1}{2})$	$2p_{1/2}2p_{3/2}^3 3p_{1/2}(J=\frac{3}{2})$	...	...
F2	13.483(6)	8.4	13.502	13.480	6.5	$2s_{1/2}(J=\frac{1}{2})$	$2s_{1/2}2p_{3/2}^3 3s_{1/2}(J=\frac{3}{2})$	...	...
F3	13.361(5)	21.7	13.376	13.361	16.7	$2s_{1/2}(J=\frac{1}{2})$	$2s_{1/2}2p_{3/2}^3 3s_{1/2}(J=\frac{3}{2})$	...	...
F4	13.310(3)	46.6	13.323	13.308	37.0	$2p_{3/2}^3(J=\frac{3}{2})$	$2p_{3/2}^2 3s_{1/2}(J=\frac{5}{2})$	13.308	13.309
F6	13.259(3)	39.2	13.267	13.256	26.9	$2p_{3/2}^3(J=\frac{3}{2})$	$2p_{3/2}^2 3s_{1/2}(J=\frac{3}{2})$	13.252	13.256
F8a	13.165(4)	11.7	13.174	13.162	7.6	$2p_{1/2}(J=\frac{1}{2})$	$2p_{1/2}2p_{3/2}^3 3s_{1/2}(J=\frac{3}{2})$	13.160	13.161
F8b	13.135(5)	8.0	13.152	13.133	5.3	$2p_{3/2}^3(J=\frac{3}{2})$	$2p_{3/2}^2 3s_{1/2}(J=\frac{1}{2})$	13.140	13.135
F9	13.078(4)	17.7	13.089	13.074	13.0	$2p_{3/2}^3(J=\frac{3}{2})$	$2p_{1/2}2p_{3/2}^3 3s_{1/2}(J=\frac{3}{2})$	13.091	13.075
F11	12.930(4)	29.3	12.940	12.926	21.8	$2p_{3/2}^3(J=\frac{3}{2})$	$2p_{1/2}2p_{3/2}^3 3s_{1/2}(J=\frac{5}{2})$	12.924	12.927
F14, 15	12.115(4)	42.0	12.114	12.108	25.3	$2p_{3/2}^3(J=\frac{3}{2})$	$2p_{3/2}^2 3d_{5/2}(J=\frac{5}{2})$	...	12.112
			12.134	12.125	12.1	$2p_{3/2}^3(J=\frac{3}{2})$	$2p_{3/2}^2 3d_{5/2}(J=\frac{3}{2})$	...	12.130
F16	12.059(6)	11.0	12.066	12.055	6.0	$2p_{3/2}^3(J=\frac{3}{2})$	$2p_{3/2}^2 3d_{5/2}(J=\frac{5}{2})$	...	...
			12.072	12.061	5.1	$2p_{3/2}^3(J=\frac{3}{2})$	$2p_{3/2}^2 3d_{3/2}(J=\frac{3}{2})$	...	...
F17	11.960(4)	27.1	11.964	11.956	24.5	$2p_{3/2}^3(J=\frac{3}{2})$	$2p_{1/2}2p_{3/2}^3 3d_{3/2}(J=\frac{5}{2})$	11.973	11.961
F19	11.869(5)	16.2	11.877	11.868	15.4	$2p_{3/2}^3(J=\frac{3}{2})$	$2p_{1/2}2p_{3/2}^3 3d_{3/2}(J=\frac{1}{2})$	...	11.874
F20	11.831(3)	100.0	11.829	11.827	65.3	$2p_{3/2}^3(J=\frac{3}{2})$	$2p_{1/2}2p_{3/2}^3 3d_{3/2}(J=\frac{5}{2})$	11.826	11.832
			11.841	11.834	34.7	$2p_{3/2}^3(J=\frac{3}{2})$	$2p_{1/2}2p_{3/2}^3 3d_{3/2}(J=\frac{3}{2})$	...	...
O0	13.838(4)	12.4	13.866	13.839	9.3	$2s_{1/2}2p_{3/2}^3(J=2)$	$2p_{3/2}3p_{3/2}(J=3)$	...	...
O1	13.492(4)	20.2	13.493	13.491	15.9	$2s_{1/2}2p_{3/2}^3(J=1)$	$2p_{1/2}2p_{3/2}^2 3p_{1/2}(J=2)$	...	...
O2	13.347(4)	48.2	13.344	13.342	42.0	$2s_{1/2}2p_{3/2}^3(J=2)$	$2p_{1/2}2p_{3/2}^2 3p_{1/2}(J=2)$	...	...
O4a	12.770(5)	9.4	12.768	12.756	7.6	$2s_{1/2}2p_{3/2}^3(J=1)$	$2s_{1/2}2p_{3/2}^2 3s_{1/2}(J=2)$	...	...
O4b	12.728(6)	9.3	12.740	12.721	11.0	$2s_{1/2}2p_{3/2}^3(J=2)$	$2s_{1/2}2p_{3/2}^2 3s_{1/2}(J=2)$	...	...
O5	12.620(4)	26.2	12.634	12.623	24.2	$2s_{1/2}2p_{3/2}^3(J=2)$	$2s_{1/2}2p_{3/2}^2 3s_{1/2}(J=2)$	...	...
O8	12.543(4)	38.1	12.552	12.541	28.7	$2p_{3/2}^2(J=2)$	$2p_{3/2}3s_{1/2}(J=2)$	...	...
O12	12.276(4)	17.2	12.284	12.274	10.5	$2p_{3/2}^2(J=2)$	$2p_{1/2}2p_{3/2}^2 3s_{1/2}(J=2)$	...	12.277
O13	12.208(4)	30.9	12.212	12.204	25.9	$2p_{3/2}^2(J=2)$	$2p_{1/2}2p_{3/2}^2 3s_{1/2}(J=3)$	...	12.208
O14	11.730(5)	16.2	11.727	11.715	4.9	$2s_{1/2}2p_{3/2}^3(J=2)$	$2s_{1/2}2p_{3/2}^2 3d_{5/2}(J=2)$	...	...
			11.754	11.738	4.3	$2s_{1/2}2p_{3/2}^3(J=2)$	$2s_{1/2}2p_{3/2}^2 3d_{5/2}(J=3)$	...	...
O16	11.652(4)	11.4	11.654	11.649	7.1	$2p_{3/2}^2(J=2)$	$2p_{3/2}3d_{3/2}(J=3)$	...	...
			11.653	11.648	4.9	$2p_{3/2}^2(J=2)$	$2p_{3/2}3d_{3/2}(J=2)$	...	...
O17	11.594(4)	14.0	11.590	11.589	10.1	$2p_{3/2}^2(J=2)$	$2p_{3/2}3d_{5/2}(J=2)$	...	...
O19	11.536(3)	36.5	11.536	11.535	46.1	$2p_{3/2}^2(J=2)$	$2p_{1/2}2p_{3/2}^2 3d_{5/2}(J=3)$	...	11.539
O22	11.421(4)	20.3	11.420	11.418	19.3	$2p_{3/2}^2(J=2)$	$2p_{1/2}2p_{3/2}^2 3d_{5/2}(J=3)$	...	...
O24	11.312(3)	100.0	11.312	11.312	100.0	$2p_{3/2}^2(J=2)$	$2p_{1/2}2p_{3/2}^2 3d_{5/2}(J=3)$	11.310	11.318
O26	11.271(3)	29.0	11.270	11.264	23.0	$2p_{3/2}^2(J=2)$	$2p_{1/2}2p_{3/2}^2 3d_{3/2}(J=1)$	...	11.272
O27	11.231(5)	5.3	11.239	11.238	8.7	$2p_{3/2}^2(J=2)$	$2p_{1/2}2p_{3/2}^2 3d_{5/2}(J=3)$	...	11.229
O28	10.916(4)	15.8	10.924	10.921	11.0	$2p_{3/2}^2(J=2)$	$2s_{1/2}2p_{3/2}^2 3p_{3/2}(J=3)$	...	...
N24	11.047(4)	28.2	11.057	11.052	17.6	$2p_{1/2}2p_{3/2}^2(J=\frac{5}{2})$	$2p_{1/2}2p_{3/2}3d_{5/2}(J=\frac{5}{2})$	...	...
			11.043	11.041	16.0	$2p_{1/2}2p_{3/2}^2(J=\frac{3}{2})$	$2p_{1/2}2p_{3/2}3d_{5/2}(J=\frac{5}{2})$	...	...
N26	10.996(4)	26.1	10.996	10.997	32.0	$2p_{3/2}(J=\frac{3}{2})$	$3d_{5/2}(J=\frac{5}{2})$	...	...
N29	10.896(4)	18.3	10.893	10.893	24.5	$2p_{3/2}(J=\frac{3}{2})$	$2p_{1/2}2p_{3/2}3d_{3/2}(J=\frac{5}{2})$	...	...
N31	10.805(4)	55.8	10.803	10.802	52.8	$2p_{3/2}(J=\frac{3}{2})$	$2p_{1/2}2p_{3/2}3d_{5/2}(J=\frac{5}{2})$	...	...
N31	10.784(4)	100.0	10.789	10.787	71.5	$2p_{3/2}(J=\frac{3}{2})$	$2p_{1/2}2p_{3/2}3d_{3/2}(J=\frac{3}{2})$	...	...
			10.780	10.779	28.5	$2p_{3/2}(J=\frac{3}{2})$	$2p_{1/2}2p_{3/2}3d_{3/2}(J=\frac{1}{2})$	...	...
N33	10.578(4)	26.2	10.585	10.578	13.3	$2p_{3/2}(J=\frac{3}{2})$	$2s_{1/2}2p_{1/2}2p_{3/2}^2 3p_{3/2}(J=\frac{5}{2})$	...	...
			10.588	10.582	10.6	$2p_{3/2}(J=\frac{3}{2})$	$2s_{1/2}2p_{3/2}3p_{3/2}(J=\frac{3}{2})$	...	...
C1	11.767(4)	19.7	11.772	11.764	21.6	$2s_{1/2}2p_{3/2}(J=1)$	$2p_{1/2}3p_{1/2}(J=0)$	...	...
C2	11.416(4)	15.8	11.416	11.412	12.8	$2s_{1/2}2p_{3/2}(J=1)$	$2p_{3/2}3p_{3/2}(J=0)$	...	...
C3	11.355(4)	19.2	11.350	11.348	17.7	$2s_{1/2}2p_{3/2}(J=1)$	$2p_{3/2}3p_{3/2}(J=0)$	...	...
C8	10.483(5)	20.4	10.486	10.484	16.0	$2p_{1/2}2p_{3/2}(J=1)$	$2p_{1/2}3d_{3/2}(J=1)$	...	...
C10	10.364(3)	100.0	10.368	10.365	100.0	$2p_{1/2}^2(J=0)$	$2p_{1/2}3d_{3/2}(J=1)$	...	...
B1	11.146(4)	16.2	11.163	11.149	16.6	$2s_{1/2}2p_{1/2}2p_{3/2}(J=\frac{3}{2})$	$3p_{1/2}(J=\frac{1}{2})$	...	...
B3	10.908(4)	15.1	10.922	10.910	14.3	$2s_{1/2}2p_{1/2}2p_{3/2}(J=\frac{1}{2})$	$2s_{1/2}2p_{1/2}3s_{1/2}(J=\frac{1}{2})$	...	...

TABLE 1—*Continued*

Label[a] (1)	λ_{exp}[b] (Å) (2)	I_{exp}[c] (3)	λ_{CI}[d] (4)	λ_{MBPT}[e] (5)	I_{cal}[f] (6)	Lower[g] (7)	Upper[h] (8)	Phillips[i] (Å) (9)	NIST[j] (Å) (10)
B9	10.128(4)	25.6	10.130	10.128	19.0	$2s_{3/2}(J=\frac{3}{2})$	$3d_{3/2}(J=\frac{3}{2})$	...	...
B13	9.962(3)	100.0	9.966	9.962	100.0	$2p_{1/2}(J=\frac{1}{2})$	$3d_{3/2}(J=\frac{3}{2})$	...	...
B19	9.688(4)	16.1	9.689	9.686	23.5	$2p_{1/2}(J=\frac{1}{2})$	$2s_{1/2}2p_{1/2}3s_{3/2}(J=\frac{3}{2})$	...	...
Be1	10.312(3)	44.7	10.319	10.308	50.4	$2s_{1/2}2s_{3/2}(J=1)$	$2s_{1/2}3s_{1/2}(J=0)$	...	...
Be2	9.967(3)	100.0	9.971	9.966	100.0	$2s_{1/2}2s_{3/2}(J=1)$	$2s_{1/2}3d_{5/2}(J=2)$	...	9.970
Be8	9.383(3)	20.9	9.386	9.384	28.1	$2s^2_{1/2}(J=0)$	$2s_{1/2}3p_{1/2}(J=1)$	...	9.390
Be9	9.347(4)	38.4	9.347	9.345	47.6	$2s^2_{1/2}(J=0)$	$2s_{1/2}3s_{3/2}(J=1)$	...	9.340
Li1	9.744(4)	68.9	9.748	9.745	51.5	$2s_{3/2}(J=\frac{3}{2})$	$3s_{1/2}(J=\frac{1}{2})$	...	...
Li3	9.528(4)	100.0	9.533	9.529	100.0	$2s_{3/2}(J=\frac{3}{2})$	$3d_{5/2}(J=\frac{5}{2})$	...	9.535

[a] The labels for Ni XIX lines follow the convention of Parkinson (1973) as modified by Beiersdorfer et al. (1988) for Ni XIX, and those for Ni XX–XXIV lines are matched to the labels of corresponding transitions of Fe XVIII–XXIV given in Brown et al. (2002).
[b] Measured wavelengths. Numbers in the parentheses are the estimated uncertainties in milliangstroms.
[c] Measured relative intensity. The strongest line of each charge state has the intensity of 100.
[d] Calculated wavelengths using the configuration interaction theory.
[e] Calculated wavelengths using the MBPT.
[f] Calculated relative intensity using FAC with the configuration interaction theory and distorted-wave collisional excitation cross sections.
[g] Configuration labels for the lower levels. Numbers in the parentheses are the total angular momenta of the levels.
[h] Configuration labels for the upper levels. Numbers in the parentheses are the total angular momenta of the levels.
[i] Wavelengths from Phillips et al. (1982).
[j] Wavelengths from the NIST atomic spectra database.

state is labeled by the configuration basis that has the dominant mixing coefficient. In cases in which more than two basis functions of the same symmetry have similar mixing coefficients, slight differences in configuration interactions may cause the label of a state to change from one configuration to another. The configuration labels for the lines O17, O22, and C3 in the present work are different from those of Brown et al. (2002). For example, in the present work, the O22 is assigned a transition between $2p^2_{3/2}(J=2)$ and $2p_{1/2}2p^2_{3/2}3d_{5/2}(J=3)$, while Brown et al. (2002) assigned it a transition between $2p^2_{3/2}(J=2)$ and $2p_{1/2}2p^2_{3/2}3d_{3/2}(J=3)$. The different orbitals, $3d_{5/2}$ and $3d_{3/2}$, in the upper level are results of different configuration interactions.

In the present measurement, two F-like lines are assigned to F8, and are labeled as F8a and F8b. Brown et al. (2002) assigned F8a as F8, and F8b as F7. However, the measured intensity of F8 in Fe was 3 times larger than the theoretical intensity of F8a. The MBPT wavelengths of F8a and F8b from Gu (2005) are very close for Fe, indicating that they both contribute to the F8 line. Inspection of the F-like Fe line list in Gu (2005) indicates that no suitable line can be assigned to F7 of Brown et al. (2002). We also find no evidence of the corresponding F7 Ni line in the present measurement. Desai et al. (2005) also noticed that the theoretical intensity of F8 line of Fe is too small as compared with the *Chandra* observations of the Capella corona, if only F8a is assigned to F8. The agreement is much better if both F8a and F8b identified here are assigned to F8. In Ni, the two transitions are separated by 0.029 Å and are resolved in the present measurement. Therefore, their wavelengths are individually measured. The two transitions O4a and O4b are resolved in the present measurement, while Brown et al. (2002) included them in the O4 blend. Two transitions are assigned to F16 and O16 in the present work, while the corresponding Fe lines in Brown et al. (2002) contain only one transition each. The configuration labels and symmetries of lower and upper levels of these Ni and Fe lines are also different. Therefore, they represent different transitions for Ni and Fe. They are assigned the same name based on their wavelengths relative to the nearby lines in the same charge state. The O0 line in the present measurement did not appear in Brown et al. (2002) for Fe, because it falls outside the wavelength coverage of that measurement. The N24 line contains two components in both the present work and Brown et al. (2002), but only one component has the same indentification in the two measurements.

Some of the Ni XIX, XX, and XXI lines have also been measured in the solar flare X-ray spectra of Phillips et al. (1982). These wavelengths are listed in Table 1, column (9) for comparison. Phillips et al. (1982) marked the majority of Ni XX line assignments as questionable, underscoring the difficulties of making reliable identifications of Ni L-shell lines in solar spectra. This illustrates the advantage of laboratory measurements with the electronic beam ion trap, where blending with Fe L-shell lines is absent. Wavelengths obtained from the NIST atomic spectra database are also shown in Table 1, column (10).

Comparison of the present measured wavelengths with the configuration interaction calculations using FAC and the MBPT results of Gu (2005) are further illustrated in Figure 6. The discrepancies

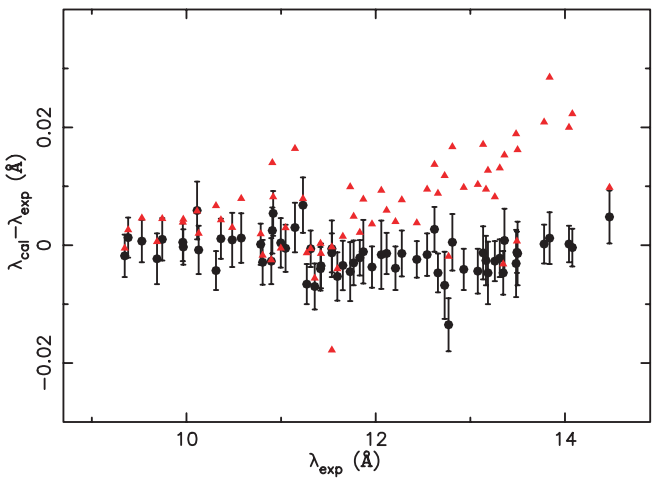

FIG. 6.—Comparison of measured wavelengths and the calculations using the configuration interaction and MBPT theories. The red triangles are the differences between the measured and configuration interaction wavelengths. The black circles are the differences between the measured and MBPT wavelengths. The error bars are the estimated uncertainties in the measured wavelengths.

between the measured and the configuration interaction wavelengths show a trend similar to those for Fe L-shell lines (see Fig. 3 of Gu 2005); i.e., the differences appear to increase with the transition wavelengths. The discrepancies for Ni lines seem to be slightly smaller than those for Fe lines. However, this is the direct result of Ni lines being at higher energies than are Fe lines and the fact that the uncertainties in the calculated transition energies are comparable for the two cases. Therefore, the uncertainties in theoretical wavelengths scale approximately as $1/\Delta E^2$. As for the Fe lines, the MBPT theory improves the agreement between the measured and calculated wavelengths of Ni lines significantly.

The measured relative intensities for each charge state agree with our theoretical model to within ~30% for most lines. Such uncertainties are typically expected for the atomic data used in the present modeling, which include only direct electron collisional excitation in the distorted-wave approximation. For a few lines, discrepancies of 30% to a factor of 2 are seen. Most of these lines are quite weak, and our cosmic-ray filtering method might have affected their measured intensities. Moreover, our assumption of flat spectrometer response may be questionable at wavelengths below 11 Å, although at longer wavelengths, Beiersdorfer et al. (2004) have verified the flatness of the spectrometer efficiency. The intensity ratios between the Ne-like lines in the present work are consistent with our earlier measurement on Ni XIX (Gu et al. 2004) and those on Fe XVII (Brown et al. 1998, 2006; Beiersdorfer et al. 2002). Specifically, the relatively strong lines, 3D, 3F, 3G, and M2, are underpredicted by up to 30% in theory relative to the 3C line, as compared with the measurement. Brown et al. (2006) have shown that this is in fact largely due to the overprediction of the 3C theoretical cross section. Similar problems may also exist for lower charge states. For example, in the present measurement, the theoretical intensities of $2p$–$3s$ transitions of F-like ion, F2–F11, are all underpredicted by 20%–30% relative to F20, a $2p$–$3d$ transition.

5. SUMMARY

We have measured the wavelengths of most strong $3 \rightarrow 2$ transitions of X-ray lines from Ni XIX to XXVI. Detailed collisional radiative modeling using the Flexible Atomic Code is used to identify transitions from different Ni L-shell charge states. The results are compared with previous measurements from solar flare X-ray observations for some Ni XIX, XX, and XXI lines. The present measurements are also compared with the calculations using the configuration interaction and many-body perturbation theories as implemented in the FAC. It is shown that MBPT significantly improves the agreement between the measured and predicted wavelengths. Combined with the previous measurements of Fe L-shell lines (Brown et al. 1998, 2002; Chen et al. 2007), this work completes the list of strong lines from L-shell ions in the soft X-ray region for incorporation into astrophysical databases.

The work at the University of California Lawrence Livermore National Laboratory was performed under the auspices of the US Department of Energy under contract W-7405-Eng-48 and supported by NASA Astronomy and Physics Research and Analysis grant NAG5-5419 to Stanford University and LLNL.

REFERENCES

Bar-Shalom, A., Klapisch, M., & Oreg, J. 2001, J. Quant. Spectrosc. Radiat. Transfer, 71, 169
Beiersdorfer, P. 2003, ARA&A, 41, 343
Beiersdorfer, P., Magee, E. W., Träbert, E., Chen, H., Lepson, J. K., Gu, M. F., & Schmidt, M. 2004, Rev. Sci. Instrum., 75, 3723
Beiersdorfer, P., et al. 1988, Phys. Rev. A, 37, 4153
———. 2002, ApJ, 576, L169
Brown, G. V., Beiersdorfer, P., Liedahl, D. A., Widmann, K., & Kahn, S. M. 1998, ApJ, 502, 1015
Brown, G. V., Beiersdorfer, P., Liedahl, D. A., Widmann, K., Kahn, S. M., & Clothiaux, E. J. 2002, ApJS, 140, 589
Brown, G. V., et al. 2006, Phys. Rev. Lett., 96, 253201
Chen, H., Gu, M. F., Behar, E., Brown, G. V., Kahn, S. M., & Beiersdorfer, P. 2007, ApJS, 168, 319
Desai, P., et al. 2005, ApJ, 625, L59
Drake, G. W. 1988, Canadian J. Phys., 66, 586
Gu, M. F. 2003, ApJ, 582, 1241
———. 2005, ApJS, 156, 105
Gu, M. F., et al. 2004, ApJ, 607, L143
Johnson, W. R., & Soff, G. 1985, At. Data Nucl. Data Tables, 33, 405
Lepson, J. K., et al. 2002, ApJ, 578, 648
Levine, M., Marrs, R., Henderson, J., Knapp, D., & Schneider, M. 1988, Phys. Scr., T22, 157
Parkinson, J. H. 1973, A&A, 24, 215
Phillips, K. J. H., et al. 1982, ApJ, 256, 774